communications physics

ARTICLE

https://doi.org/10.1038/s42005-022-00833-2 OPEN

Magnetization-driven Lifshitz transition and charge-spin coupling in the kagome metal YMn_6Sn_6

Peter E. Siegfried[1,2✉], Hari Bhandari[1,2], David C. Jones[1,2], Madhav P. Ghimire[3,4], Rebecca L. Dally[5], Lekh Poudel[5,6], Markus Bleuel[5,6], Jeffrey W. Lynn[5], Igor I. Mazin[1,2] & Nirmal J. Ghimire[1,2✉]

The Fermi surface (FS) is essential for understanding the properties of metals. It can change under both conventional symmetry-breaking phase transitions and Lifshitz transitions (LTs), where the FS, but not the crystal symmetry, changes abruptly. Magnetic phase transitions involving uniformly rotating spin textures are conventional in nature, requiring strong spin-orbit coupling (SOC) to influence the FS topology and generate measurable properties. LTs driven by a continuously varying magnetization are rarely discussed. Here we present two such manifestations in the magnetotransport of the kagome magnet YMn_6Sn_6: one caused by changes in the magnetic structure and another by a magnetization-driven LT. The former yields a 10% magnetoresistance enhancement without a strong SOC, while the latter a 45% reduction in the resistivity. These phenomena offer a unique view into the interplay of magnetism and electronic topology, and for understanding the rare-earth counterparts, such as $TbMn_6Sn_6$, recently shown to harbor correlated topological physics.

[1] Department of Physics and Astronomy, George Mason University, Fairfax, VA 22030, USA. [2] Quantum Science and Engineering Center, George Mason University, Fairfax, VA 22030, USA. [3] Central Department of Physics, Tribhuvan University, Kirtipur, Kathmandu 44613, Nepal. [4] Leibniz Institute for Solid State and Materials Research, IFW Dresden, Helmholtzstr. 20, D-01069 Dresden, Germany. [5] NIST Center for Neutron Research, National Institute of Standards and Technology, Gaithersburg, MD 20899, USA. [6] Department of Materials Science and Engineering, University of Maryland, College Park, MD 20742, USA. ✉email: psiegfri@gmu.edu; nghimire@gmu.edu

Conventionally, a phase transition is marked by the onset of an order parameter due to a spontaneously broken symmetry. Typically the order parameter is related to some thermodynamic quantity, e.g. magnetization, density, or polarization, that grows continuously after the transition. A Lifshitz transition (LT), on the other hand, is a unique electronic transformation in metals associated with a change in the Fermi surface (FS) topology[1] that occurs without breaking any symmetries, and as such, LTs driven by a continuously changing magnetization are quite rare. The effect, however, is enhanced with the lowering of the effective dimension of the FS pocket involved and can play an important role in stabilizing new types of topological phases[2–4]. In contrast, conventional field induced transitions concerning changes in magnetic texture (1st or 2nd order) involve a uniform rotation in spin space. Their effect on the electronic structure, and therefore on the transport properties, is controlled solely through the relativistic spin-orbit interaction, which is weak, determined by the fine structure constant $\alpha \simeq 1/137$, but grows with atomic number, Z. Typically a strong spin-orbit coupling (SOC) is required to observe magnetotransport signatures in this case. Here we show that the kagome lattice magnet YMn_6Sn_6 is a prototype system in terms of electronic transport that shows the two above mentioned magnetotransport properties. First, it exhibits a magnetization driven LT, with a strong effect on the c-axis conductivity, and second, a sizable electron-spin coupling without a strong SOC.

Results and discussion

Magnetization and magnetic structure. YMn_6Sn_6 is a ternary kagome magnet, a family of materials known to host a variety of topological states and phenomena[5–8]. It crystallizes in the hexagonal space group P6/mmm (#191)[9] with Mn atoms forming a kagome net in the basal plane as depicted in Fig. 1a and b. The material orders antiferromagnetically at 340 K and quickly transitions into an incommensurate spiral below 333 K. At all temperatures, a magnetic field applied along the c-axis cants the moments lying in the ab-plane towards the c-axis, while for a magnetic field applied in the ab-plane, a series of competing phases[10–12] are formed, as depicted in Fig. 1c (see Supplementary Note 2 for details). A schematic plot of the different magnetic structures and their wavevectors is shown in Fig. 1d. Application of a magnetic field in the ab-plane first cants the spins rotating in the ab-plane, creating a distorted spiral phase, characterized by the wavevector $k = (0, 0, 0.26)$. When the magnetic field reaches H_1, the spins flop to the perpendicular plane and cant towards the direction of the external field, maintaining the incommensurate c-axis spiral with only a slight increase in the spiral wavevector ($k_z = 0.27$). This phase is a transverse conical spiral. When the field reaches H_2, the spins flop back into the ab-plane forming a commensurate fan-like phase. A projection of the fan-like spins onto the direction of the magnetic field (x-component) and along the perpendicular direction in the ab-plane results in a spin pattern repeating every two and four unit cells, respectively (see Supplementary Fig. 3), producing two different commensurate Bragg peaks observed in neutron diffraction at $k_z = 0.5$ and 0.25, as shown schematically by the red lines in Fig. 1d. At H_3 the moments saturate to form the forced ferromagnetic phase.

Magnetotransport. Magnetoresistance (MR) at 1.8 K is plotted on the left axes of Fig. 2a and b. To compare the MR with the underlying magnetism, corresponding magnetization data are plotted in each figure on the right axis (see Supplementary Note 3 for the sensitivity of resistivity to the magnetic ordering with temperature). For the field applied in the ab-plane presented in panel (a), magnetization (black) shows a spin-flop transition at 2.2 T (H_1) corresponding to the distorted spiral - transverse conical spiral phase transition and a slope change slightly above 6.5 T (H_2) where the transverse conical spiral - fan like phase transition occurs. When current is applied in the ab-plane ($MR_{I_{ab}}$) (blue), the MR shows a small jump at 2.2 T (H_1), a small slope change at 4.5 T, and a sharp drop quickly above 8 T. The decrease in $MR_{I_{ab}}$ above 8 T can be understood as polarization of the fan-like spins in the direction of the magnetic field, reducing spin fluctuations and the electron scattering. The slope change at 4.5 T has no corresponding change in the magnetization and is a small feature in this measurement configuration. In contrast, the MR with current along c (MR_{I_c}) (red) shows three remarkable features. First, there is no noticeable jump at H_1 despite the magnetic phase transition with a significant increase in

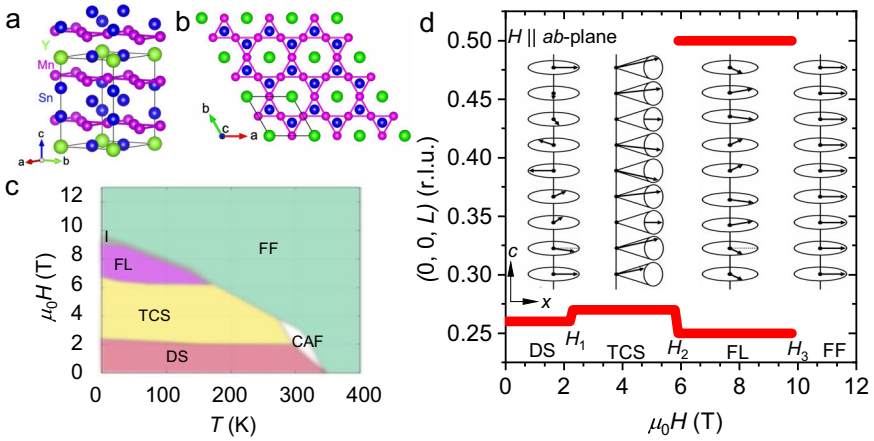

Fig. 1 Crystal structure and magnetic properties of YMn_6Sn_6. a Crystal structure of YMn_6Sn_6. **b** c-axis view of the structure showing Mn atoms arranged in a kagome-net in the ab-plane. **c** Schematic temperature (T) and magnetic field (H) phase diagram of YMn_6Sn_6 labeled for the various magnetic phases for field applied in the ab-plane including the distorted spiral (DS), transverse conical spiral (TCS), fan-like (FL), and forced ferromagnetic (FF) phases. Small pockets labeled as I and CAF represent phase I and the canted antiferromagnetic phase, respectively. **d** Plot of the wavevector ($L = k_z$) of the magnetic Bragg peaks observed in neutron diffraction experiments at 10 K (red lines) and illustrations of the magnetic structures for DS, TCS, FL, and FF phases. Magnetic fields at which transitions from DS to TCS, TCS to FL, and FL to FF are indicated by H_1, H_2, and H_3, respectively. Arrows represent the direction of spins in each Mn-layer. The labels c and x represent c-axis and the direction of magnetic field in the ab-plane, respectively.

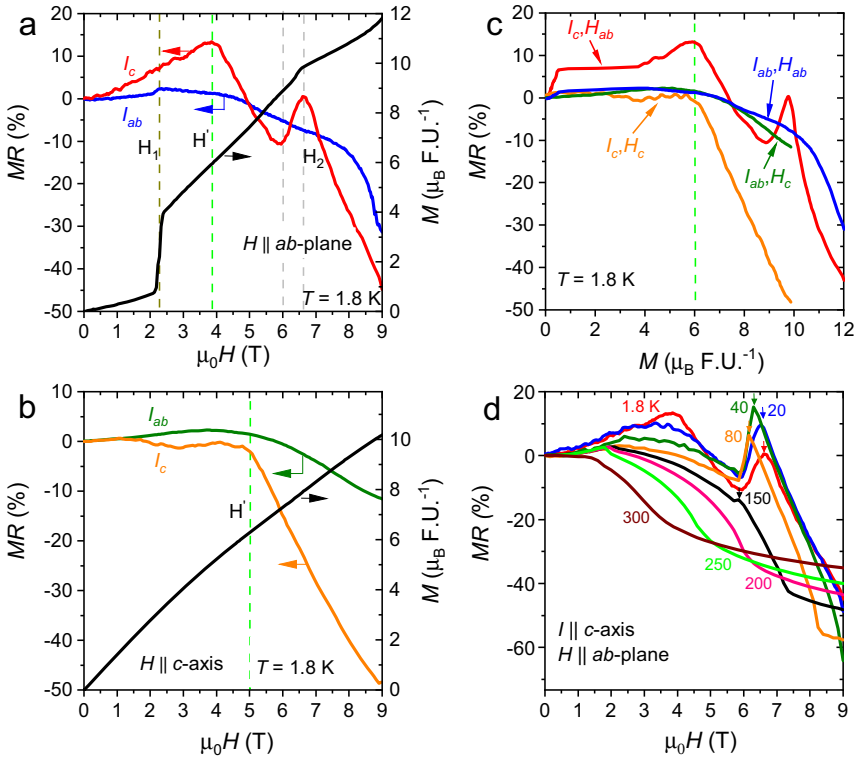

Fig. 2 Magnetoresistance, and magnetization of YMn_6Sn_6. a, **b** Magnetoresistance (MR) at 1.8 K for current along the *c*-axis, I_c, and in the *ab*-plane, I_{ab}, and the magnetization, *M*, as a function of magnetic field, *H*. *H* is applied in the *ab*-plane in panel (**a**), and along the *c*-axis in panel (**b**). Dark gray dashed lines indicate transitions from the distorted spiral to transverse conical spiral phase (H_1) and light gray dashed lines indicate the transition from transverse conical spiral to fan-like phase (H_2). Green dashed lines corresponds to the MR turnover (H'). **c** MR as a function of *M* at 1.8 K. The symbols H_c, and H_{ab} refer to the magnetic field applied along the *c*-axis and in the *ab*-plane, respectively. Green dashed line shows the MR turnover at H' occurs at 6 μ_BF.U.$^{-1}$ independent of applied field direction. Demagnetization considerations are discussed in Supplementary Note 1. **d** MR for I_c and H_{ab} at the indicated temperatures. The arrows track the MR peak at H_2.

magnetization. Second, MR_{I_c} drops sharply at 4 T with no corresponding change in magnetization. Third, it again increases sharply, by about 10% at 6 T, peaks at H_2, and then again drops sharply.

MR and magnetization with the magnetic field along the *c*-axis are presented in Fig. 2b. Here, the magnetization smoothly increases up to 9 T indicating a continuous canting of the spins towards the *c*-axis. MR for current in the *ab*-plane ($MR_{I_{ab}}$) (green) initially increases, reaching a maximum at 4.5 T and then decreases with a smaller overall change (~8%) in MR. The drop for MR with the current applied along the *c*-axis MR_{I_c} (orange) is much larger (45%) beginning at 5 T. We refer to this magnetic field, where MR drops without a corresponding change in magnetization, as H'.

In Fig. 2c, the MRs measured in all four configurations at 1.8 K are plotted together as a function of the corresponding magnetic moment. The plot shows that the H' MR drop occurs, irrespective of orientation, when the magnetization reaches 6 μ_BF.U.$^{-1}$, indicating that the H' MR drop is magnetization induced. The highly anisotropic nature of this H' feature, indicated by a larger change for current along the *c*-axis than in the *ab*-plane, suggests that the electronic state driving it is highly anisotropic. It is to be noted that the small jump in MR_{I_c} with field in the *ab*-plane (red curve) at 1 μ_BF.U.$^{-1}$ of *M* is related to the sudden increase in *M* at H_1. The temperature evolution of the MR_{I_c} for the in-plane field is depicted in Fig. 2d for selected temperatures. The full temperature range measured for each of the current and applied field configurations is discussed in Supplementary Note 4. The H' drop in MR starts broadening at 20 K and disappears above 40 K. A typical reason for a drop in magnetoresistance (or negative magnetoresistance) is suppression of spin fluctuations by the magnetic field. However, in our case several experimental observations preclude such an explanation for the H'-MR drop. First, the negative MR related to suppression of spin fluctuation should be more pronounced closer to the transition temperature, while it is exactly the opposite in our case. Second, the H'-MR drop is highly anisotropic with respect to the in- and out-of plane currents, but the H'-MR signature occurs exactly when the magnetization reaches 6 μ_BF.U.$^{-1}$, regardless of the direction of the applied magnetic field, and despite the fact that the magnetic fields along *c*-axis and in the *ab*-plane stabilize different magnetic structures: gradual spin canting towards the *c*-axis, and a transverse conical spiral, respectively. Third, thermal conductivity measured as a function of temperature peaks at 38 K and sharply decreases below this temperature (see Supplementary Note 5), suggesting that the phonons are being frozen out below 38 K, leaving the electronic contribution to the thermal conductivity as the primary source of heat transport. This behavior matches with the temperature dependence of the H'-MR drop that disappears above 40 K due to thermal activation of phonons and increased phonon scattering. The H_2 MR peak follows the fan-like phase shown in the phase diagram in Fig. 1c. The peak persists to 150 K and disappears by 200 K, matching with the fan-like phase boundary at 170 K[10].

Thus, we conclude that the observed MR features are triggered by some changes in the electronic structure. In order to relate those to the microscopic magnetic structure, we plot the 1.8-K

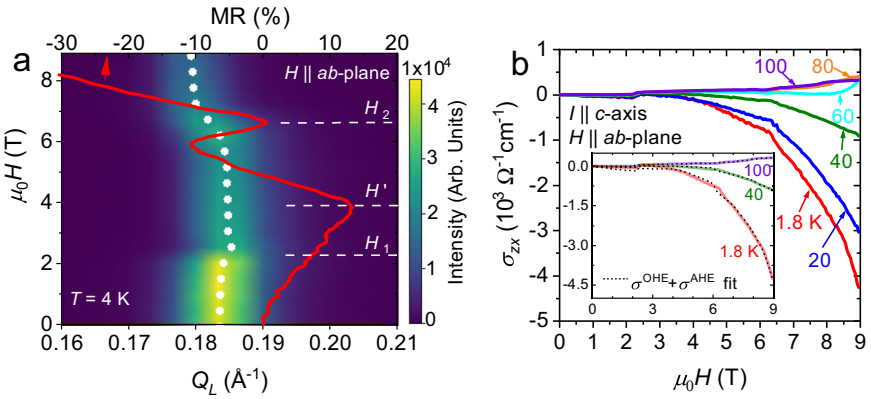

Fig. 3 Magnetotransport and small angle neutron scattering intensity of YMn_6Sn_6. a Neutron intensity-Q map of the magnetic field dependence of the magnetic Bragg peak observed in small angle neutron scattering, adapted from Ghimire, et al.[10, 20], plotted together with the magnetoresistance (MR) for current along the *c*-axis. Q_L refers to the *z*-component of the scattering vector, Q. In both cases, magnetic field is applied in the *ab*-plane. The white dots are a guide to the peak center. White dashed lines locate the magnetic structure transitions indicated by H_1 and H_2 and the MR turnover at H'. **b** Hall conductivity, σ_{zx}, as a function of magnetic field, *H*, at indicated temperatures. Inset depicts the fits (black dotted lines) of the Hall conductivity comprised of only ordinary, $\sigma^{OHE} = R_H H \rho_{zz}^{-1} \rho_{xx}^{-1}$, and anomalous, $\sigma^{AHE} = S_H M$, conductivity contributions, where R_H is the ordinary Hall coefficient, and S_H is the anomalous Hall coefficient, *M* is the magnetization vs field applied in the *ab*-plane, and ρ_{zz} and ρ_{xx} are the longitudinal resistivities for current applied along the *c*-axis and current applied in the *ab*-plane, respectively.

MR_{I_c} for the in-plane magnetic field together with the magnetic Bragg peak measured using small angle neutron scattering at 4 K in Fig. 3a. The intensity of the Bragg peak does not show a noticeable change below H_1. At H_1, the Bragg peak loses intensity and the wavevector slightly increases marking the distorted spiral - transverse conical spiral phase transition. There is no apparent change in the intensity or the wavevector at H', the MR turnover field, signifying no change in magnetic structure at H' besides a gradual spin canting. The H_2 peak in MR corresponds exactly to the region where the wavevector of the magnetic Bragg peak changes at the transverse conical spiral to fan-like phase boundary. Once in the fan-like phase, the MR starts decreasing as the magnetic field starts canting the spins along the field. These observations unambiguously show that the H' MR drop and H_2 MR peak are associated with the magnetic field induced changes in the electronic and magnetic structures, respectively, with the former being magnetization driven indicating an LT. An LT is usually accompanied by a change in carrier concentration observable through Hall effect measurements. However, we do not see a noticeable slope change in the Hall conductivity (Fig. 3b) or resistivity (Supplementary Fig. 9) at H', but rather a gradual change. This paradox can be related to the complex fermiology of a metal with a complicated band structure (see Supplementary Note 6). Note that while magnetoresistance and Hall conductivity are closely related, a 10% change (the immediate change at H') in the former does not necessarily correspond to a measurable change in the latter, especially when it is dominated by the anomalous term, as in this case (see Supplementary Note 7).

Microscopic origin of magnetoresistance signatures. To investigate the microscopic origin of the LT, we calculated the non-relativistic electronic band structure in the experimental zero-field zero-temperature spiral magnetic phase and in the fully polarized ferromagnetic state. Ferromagnetic band structure calculations suggested that the effect of SOC on the band dispersions is, expectedly, rather weak in YMn_6Sn_6, so most of the reported calculations were performed without SOC. In the zero-field state (blue bands), there are no bands at the Fermi energy (E_F) at the *L*-point as depicted in Fig. 4a. On the contrary, in the polarized state, a flat band from the spin majority channel appears at E_F, emphasized in bold in Fig. 4a. It forms a highly anisotropic hole pocket around *L*, visible as a pancake shape in Fig. 4b, where the Fermi surface for the spin majority bands is depicted. This hole pocket is highly dispersive along *c*, nearly flat in the $L-A$ direction and rather heavy along $L-H$. Due to its quasi-1D nature, this hole pocket contributes mainly to the transport along *c*. Other features of the Fermi surface include one large electron pocket around *H* and one large hole pocket around *K*, forming two networks of interconnected triangular pillows. These pockets are also more dispersive along *c*, but are much less anisotropic than the hole pocket around *L*. In addition, there are also two small electron pockets: one between *L* and *M*, a remnant of a quasi-2D band, and another around Γ. Overall, somewhat counterintuitively for the layered structure of YMn_6Sn_6, the spin-up electrons propagate more easily perpendicular to the Mn planes. Spin-down bands, on the contrary, prefer the in-plane transport. It can be inferred that the new Fermi surface appears, via an LT, well below full saturation, i.e., when the moments attain a value of $M = 6\mu_B$F.U.$^{-1}$ at H', and is responsible for the sharp drop in MR. This is consistent with the fact that the drop occurs at different field magnitudes for the in-plane and out-of-plane field directions, but at the same *M*, and is considerably more pronounced for the *c*-axis MR. We emphasize that the electronic structure is sensitive to the direction of the spin polarization only as much as the SOC (tens of meV) is strong compared to the non-relativistic electron energy (eVs). Thus in a material with a weak SOC, such as this compound, the change in the Fermi surface occurs independent of the direction of polarization, as observed in the H'-MR drop occurring when the moments attain a value of $M = 6\mu_B$F.U.$^{-1}$, regardless of the direction of spin polarization.

Turning attention to the H_2-MR peak that occurs during the transverse conical spiral to fan-like phase transition, we calculate the hopping probabilities (which in turn determine the conductivities) in each of the phases within a tight-binding approximation. For a 1D chain, the probability for an electron to travel along the chain is determined by the lowest of the individual probabilities which we call the bottleneck. The hopping between two electrons with non-parallel spins is proportional to half of the cosine of the angles between them. The experimentally

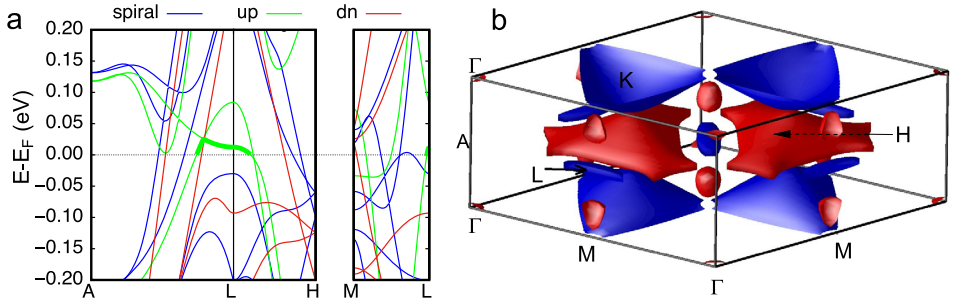

Fig. 4 Electronic band structure and Fermi surface of YMn_6Sn_6. a Calculated electronic band structure near the Fermi energy, E_F, at the *L* point of YMn_6Sn_6 in the magnetic spiral ground state, (blue lines) and in the spin polarized state. The lines with green, and red color represent spin up (up) and spin down (dn) bands, respectively. All calculated bands are shown in Supplementary Fig. 8. **b** Calculated Fermi surface around Γ, *M* and *L* points.

determined largest angles between two spins in the transverse conical spiral and fan-like phases are 67.9°, and 81°, respectively[11] [see Supplementary Note 8 for details]. Thus, the bottleneck factor in the transverse conical spiral and fan-like phases for the *c*-axis transport is 0.83, and 0.76, respectively. The bottleneck factor along *c* (but not in-plane) in the transverse conical spiral phase is 9% higher than that in the fan-like phase, quantitatively accounting for the 10% rise of the interplaner magnetoresistance. It is to be noted here that this effect is entirely due to the spin texture and not to the SOC, as evidenced by a negligible MR for a much larger magnetization change at H_1. Such an interplaner MR has been discussed with respect to the chiral solition lattice phase in $Cr_{1/3}NbS_2$[13], where the Dzyaloshinskii-Moriya interaction driven chirality is inherently coupled to the SOC. The charge-spin coupling in YMn_6Sn_6 is unique in that it requires neither chirality nor a strong SOC.

Common LTs, driven by doping, strain, or pressure, are often associated with van Hove singularities[14] that are difficult to observe via transport measurements. Moreover, those LTs are rather inflexible, since chemical doping cannot be controlled in situ within the same sample, and varying strain or pressure appreciably is difficult. An uncommon magnetization driven LT is free of these shortcomings, and has potential as a tool to tune the FS topology. We emphasize that while this specific LT is rather fortuitous, considerable modification of the FS via applied field in spiral magnets is to be expected, and it is likely that similar LTs will be discovered in other spiral magnets. The magnetic transition at H_2, which occurs between two ordered phases, as opposed to the spin-flop transition at H_1, does affect the MR (but only along c), as shown in Fig. 2a. The scale of this effect can be estimated from the standard formula relating the one-electron hopping probability to the angle between the local magnetic moments[15] and is consistent with the experimental change in MR. This behavior marks the electron-spin interaction without the requirement of strong SOC or spin chirality, as in the chiral magnets[13, 16].

Conclusions

In summary, our magnetotransport measurements in varying applied magnetic fields, and in different current directions, uncover two nontrivial effects in magnetoresistance. Using first principles calculations, we were able to identify one of them, which occurs at a magnetization of $M = 6\mu_B$F.U.$^{-1}$ for any field direction, as a magnetization driven Lifshitz transition, qualitatively different from common pressure or strain driven ones. The other effect demonstrates how magnetotransport phenomena are intimately related to the change in magnetic texture. These types of effects are strongly desired for potential spintronic applications and, thus, our results provide a compelling observation to stimulate new theoretical and experimental research into the interaction between the topology of electronic bands in kagome lattices, magnetic interactions, and spin-orbit coupling, especially in the rare-earth ternary kagome magnet systems.

Methods

Single crystal growth. Single crystals of YMn_6Sn_6 were grown by the self-flux method. Y pieces (Alfa Aesar; 99.9%), Mn pieces (Alfa Aesar; 99.95%), and Sn shots (Alfa Aesar; 99.999%) were loaded in a 2-ml aluminum oxide crucible in a molar ratio of 1:1:20. The crucible was sealed in a fused silica ampoule under vacuum and heated to 1175 °C over 10 h, homogenized at 1175 °C for 12 h, and then cooled to 600 °C over 100 h. Upon reaching 600 °C the excess flux was decanted from the crystals using a centrifuge leaving behind well-faceted hexagonal crystals up to 100 mg in mass. All measurements were performed on crystals oriented for the [0, 0, 1] and [1, 1, 0] directions.

Transport and magnetization. For electrical transport measurements samples were polished to dimensions of ~$1.00 \times 0.40 \times 0.15$ mm with the long axis corresponding to either the *c*-axis, or the in-plane, [1, 1, 0], direction. An excitation current of 4 mA was used in all measurements presented. Identical data were also measured with a 2 mA excitation, however, the higher 4 mA current produced less noise without impacting the features observed. Electrical contacts were affixed using Epotek H20E silver epoxy and 25 μm Pt wires with typical contacts resistances of ≈ 20 Ω, such that current was directed along the *c*-axis or in the *ab*-plane. MR and Hall effect data were collected using the resistivity option and rotator within a Quantum Design DynaCool PPMS equipped with a 9 T magnet. MR is defined as $MR = (\rho(H) - \rho(0))/\rho(0)$, where $\rho(H)$ and $\rho(0)$ are the longitudinal resistivity with and without an applied magnetic field, *H*. The Hall resistivity was asymetrized from the positive and negative applied magnetic fields via $\rho_{xz} = [\rho_T(+H) - \rho_T(-H)]/2$, where ρ_T is the resistivity measured via the transverse voltage contacts in the Hall bar geometry. Hall conductivity for current along the *c*-axis was calculated via the relation $\sigma_{zx} = \rho_{xz}/(\rho_{xz}^2 + \rho_{zz}\rho_{xx})$. Here, ρ_{zz} is the longitudinal resistivity for current along the *c*-axis and magnetic field in the *ab*-plane, ρ_{xx} is the longitudinal resistivity for mutually perpendicular current and magnetic field in the *ab*-plane, and ρ_{xz} is the Hall resistivity for current along *c*. It is to be noted that the $\rho_{zz}\rho_{xx}$ term in the denominator is due to the anisotropy in ρ_{xx} and ρ_{zz} in the hexagonal system as evident in Supplementary Fig. 4. The fits of the Hall conductivity were piecewise above and below H_2, where the transverse conical spiral to fan-like transition imparts a significant change to the electronic structure and hence the Hall conductivity. DC magnetization measurements were performed in the same PPMS system using the ACMS II option.

Small angle neutron scattering. Small Angle Neutron Scattering data were collected with the NG-7 SANS instrument at the NIST Center for Neutron Research using a 9 T horizontal field magnet (H||[1, 1, 0]) and in the temperature range from 4 K to 300 K. For Fig. 3a, conversion of wavevector to Å^{-1} from r.l.u units is made through the following relation, $Q_L(Å^{-1}) = 2\pi L/c$, where *L* is the *z*-component of the wavevector in r.l.u. [k = (*H*, *K*, *L*)], and *c* is the *c*-axis unit vector length in Å.

First-principles calculations. Most calculations were performed using the projected augmented wave pseudo-potential code VASP[17] and the gradient-dependent density functional of Perdew, et al.[18]. For control purposes, some calculations were also repeated using the all-electron linearized augmented plane wave code WIEN2k[19].

Data availability

The authors declare that the main data supporting the findings of this study are available within the article and its Supplementary Information files. Extra data are available from the corresponding author upon request.

Received: 22 November 2021; Accepted: 14 February 2022;
Published online: 15 March 2022

References

1. Lifshitz, I. M. Anomalies of electron characteristics of a metal in the high pressure region. *Sov. Phys. JETP* **11**, 1130–1135 (1960).
2. Volovik, G. E. Exotic Lifshitz transitions in topological materials. *Phys.-Uspekhi* **61**, 89 (2018).
3. Okada, Y. et al. Observation of Dirac Node formation and mass acquisition in a topological crystalline insulator. *Science* **27**, 1496–1499 (2013).
4. Zeljkovic, I. et al. Mapping the unconventional orbital texture in topological crystalline insulators. *Nat. Phys.* **10**, 572–577 (2014).
5. Kitaori, A. et al. Emergent electromagnetic induction beyond room temperature. *Proc. Natl Acad. Sci.* **118**, e2105422118 (2021).
6. Li, M. et al. Dirac cone, flat band and saddle point in kagome magnet YMn_6Sn_6. *Nat. Commun.* **12**, 1–8 (2021).
7. Yin, J. X. et al. Quantum-limit Chern topological magnetism in $TbMn_6Sn_6$. *Nature* **583**, 533–536 (2020).
8. Zhang, H. et al. Topological magnon bands in a room-temperature kagome magnet. *Phys. Rev. B* **101**, 100405 (2020).
9. Mazet T. et al. A study of the new $HfFe_6Ge_6$-type $ZrMn_6Sn_6$ and $HfMn_6Sn_6$ compounds by magnetization and neutron diffraction measurements. *J Alloys Comp.* **284**, 54–59 (1999).
10. Ghimire, N. J. et al. Competing magnetic phases and fluctuation-driven scalar spin chirality in the kagome metal YMn_6Sn_6. *Sci. Adv.* **6**, eabe2680 (2020).
11. Dally, R. L. et al. Chiral properties of the zero-field spiral state and field-induced magnetic phases of the itinerant kagome metal YMn_6Sn_6. *Phys. Rev. B* **103**, 094413 (2021).
12. Wang, Q. et al. Field-induced topological Hall effect and double-fan spin structure with a *c*-axis component in the metallic kagome antiferromagnetic compound YMn_6Sn_6. *Phys. Rev. B* **103**, 014416 (2021).
13. Togawa, Y. et al. Interlayer magnetoresistance due to chiral soliton lattice formation in hexagonal chiral magnet $CrNb_3S_6$. *Phys. Rev. Lett.* **111**, 197204 (2013).
14. Sunko, V. et al. Direct observation of uniaxial stress-driven Lifshitz transition in Sr_2RuO_4. *npj Quantum Mater.* **4**, 1–7 (2019).
15. Khomskii, D. I. *Basic Aspects of the Quantum Theory of Solids: Order and Elementary Excitations*. Cambridge University Press (2010).
16. Neubauer, A. et al. Topological Hall Effect in the *A* Phase of MnSi. *Phys. Rev. Lett.* **102**, 186602 (2009).
17. Kresse, G. & Furthmüller, J. Efficient iterative schemes for ab initio total-energy calculations using a plane-wave basis set. *Phys. Rev. B* **54**, 11169 (1996).
18. Perdew, J. P., Burke, K. & Ernzerhof, M. Generalized gradient approximation made simple. *Phys. Rev. Lett.* **77**, 3865 (1996).
19. Blaha, P. et al. *An augmented plane wave plus local orbitals program for calculating crystal properties*. Vienna Univiversity of Technology (2001).
20. Figure adapted from Ghimire et al. *Science Advances*, 18 Dec 2020, Vol **6**, Issue 51, DOI: 10.1126/sciadv.abe2680.© the Authors, some rights reserved; exclusive licensee AAAS. Distributed under a CC BY-NC 4.0 license http://creativecommons.org/licenses/by-nc/4.0/.

Acknowledgements

Crystal growth and properties characterization work at George Mason University was supported by the U.S. Department of Energy, Office of Science, Basic Energy Sciences, Materials Science and Engineering Division. I.I.M. acknowledges support from the U.S. Department of Energy through the grant #DE-SC0021089. M.P.G. acknowledges the Alexander von Humboldt Foundation, Germany for the equipment grants. Access to the NG-7 SANS instrument was provided by the Center for High Resolution Neutron Scattering, a partnership between the National Institute of Standards and Technology and the National Science Foundation under Agreement No. DMR-2010792. The identification of any commercial product or trade name does not imply endorsement or recommendation by the National Institute of Standards and Technology. We thank J.F. Mitchell for useful discussions.

Author contributions

N.J.G. and P.E.S. conceived the idea. P.E.S. performed magnetic and magnetotransport measurement and carried out the data analysis. H.B. synthesized single crystals. D.C.J. contributed to the figure preparation. R.L.D., L.P. and J.W.L. contributed to neutron diffraction experiments. L.P., N.J.G., J.W.L. and M.B. performed SANS experiment. I.I.M. and M.P.G. contributed to the DFT calculations. P.E.S. and N.J.G. wrote the manuscript. All authors contributed to the discussion of the results.

Competing interests

The authors declare no competing interests.

Additional information

Supplementary information The online version contains supplementary material available at https://doi.org/10.1038/s42005-022-00833-2.

Correspondence and requests for materials should be addressed to Peter E. Siegfried or Nirmal J. Ghimire.

Peer review information *Communications Physics* thanks Shuang Jia and the other, anonymous, reviewer(s) for their contribution to the peer review of this work.

Reprints and permission information is available at http://www.nature.com/reprints

Publisher's note Springer Nature remains neutral with regard to jurisdictional claims in published maps and institutional affiliations.

Supplementary Information for: Magnetization-driven Lifshitz transition and charge-spin coupling in the kagome metal YMn_6Sn_6

Peter E. Siegfried, Hari Bhandari, David C. Jones, Madhav P. Ghimire, Rebecca L. Dally, Lekh Poudel, Markus Bleuel, Jeffrey W. Lynn, Igor Mazin, Nirmal J. Ghimire

Supplementary Note 1 Demagnetization Considerations.

Supplementary Table 1: Values used in calculating the demagnetization corrections in field for the transport measurements.

	N	m (kg)	$M^{9T,1.8K}$ (Am^{2}kg^{-1})	$4\pi 10^{-7} N \frac{mM}{V}^{9T,1.8K}$ (T)	$H_d^{9T,1.8K}$ (T)
I_{ab}, H_{ab}	0.0909	3.09×10^{-6}	57.7	0.0499	8.95
I_c, H_c	0.1901	1.48×10^{-6}	51.1	0.0958	8.90
I_{ab}, H_c	0.7440	3.09×10^{-6}	51.1	0.3749	8.63
I_c, H_{ab}	0.5567	1.48×10^{-6}	57.7	0.3056	8.69

Demagnetization corrections to the applied field take the form of $\mu_0 H_d = \mu_0 H - 4\pi \times 10^{-7} N \frac{Mm}{V}$, where $\mu_0 H_d$ is the demagnetization corrected field in T, $\mu_0 H$ is the applied field in T, N is the unitless demagnetization coefficient, M is the mass magnetization measured in Am^{2}kg^{-1}, m is the sample mass in kg, and V is the sample volume in m^3. For our transport samples we can calculate the demagnetization coefficient of the rectangular samples[1]. The calculated demagnetization corrections are shown in Supplementary Table 1. The values for H_d in Supplementary Table 1 are the maximum field corrections for our data at 9 T, such that for an applied field of 9 T the I_{ab} and H_c sample would be at an effective field of 8.63 T. These corrections are proportional to the magnetization and would be smaller at lower fields (i.e. with lower magnetization). For a linear interpolation of this factor using the largest demagnetization coefficient (I_{ab}, H_c), which is a close approximation for the magnetization as a function of field for this orientation, the correction is only

$\approx$0.2 T at an applied field of 5 T. The separation in the H' peaks between the two applied field orientations was $\approx$1 T, much larger than the maximum 0.2 T correction. All other configurations will have smaller corrections than this.

Estimating the corrections in the magnetization vs field data, is made more difficult by the hexagonal plate geometry. The correction would however only be a maximum of $\approx 30\%$ larger assuming the largest possible demagnetization coefficient of 1 for the H_c orientation, and would be much smaller in the the H_{ab} orientation due to the plate like shape of the YMn_6Sn_6 crystals. Correcting for demagnetization would shift both the transport and the magnetization data to similarly lower fields, and thus the comparison in the main text between MR vs H and M vs H wouldn't be significantly affected.

Supplementary Note 2 Susceptibility and Temperature Evolution of Magnetization.

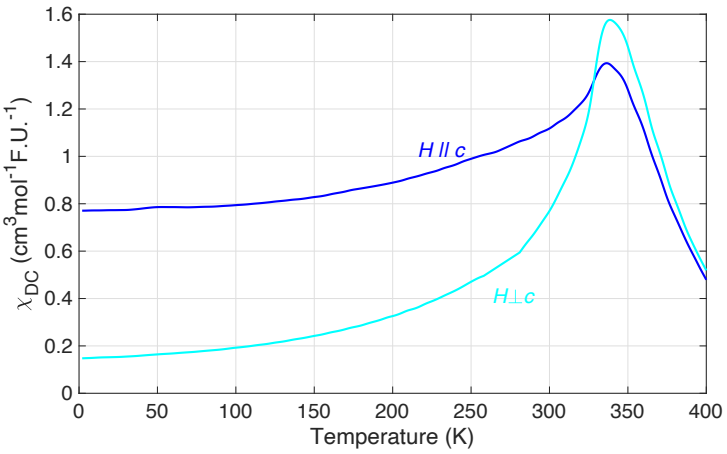

Supplementary Figure 1: Magnetic susceptibility, χ_{DC}, for YMn_6Sn_6 as a function of temperature at 0.01 T with field, H, applied in the ab-plane and along the c-axis. Peaks in both orientations identify T_{N} at 340 K for this sample.

Magnetic susceptibility measured with magnetic field of 0.01 T along c-axis and in the ab-plane is depicted in Supplementary Figure 1. The susceptibility peaks mark the Néel temperature for our samples at 340 K, in agreement with previous measurements[2,3].

Temperature evolution of magnetization for the magnetic field applied along the c-axis and in the ab-plane is presented in Supplementary Figure 2. Supplementary Figure 2 (b) shows that both H_1, the signature of the distorted spiral-transverse conical spiral transition, and the kink indicating the forced ferromagnetic phase evolve to lower fields as temperature increases, consistent with previous measurements [2,4].

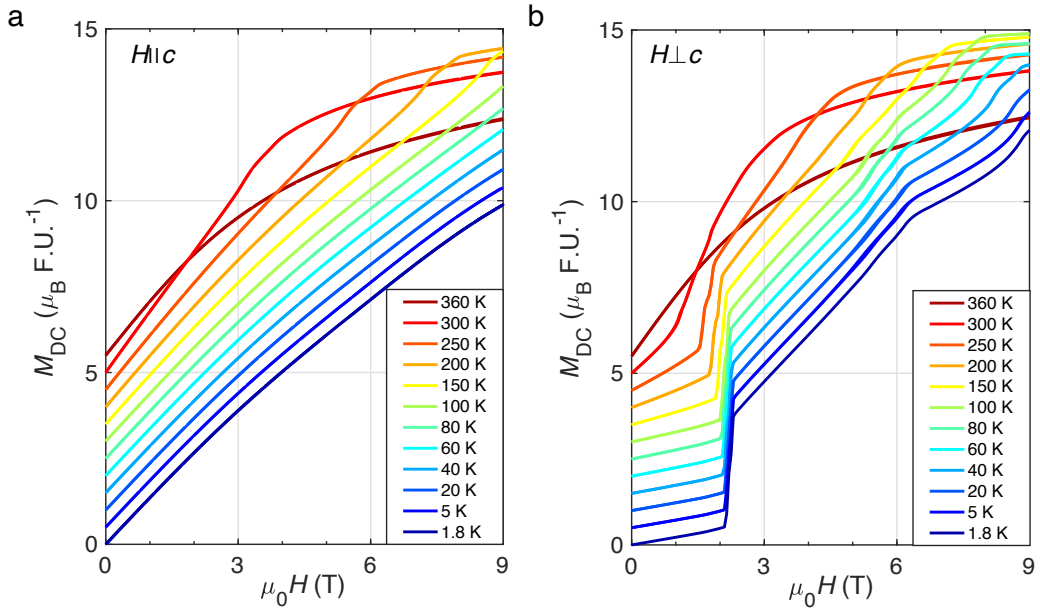

Supplementary Figure 2: DC magnetization, M_{DC}, measurements as a function of applied field, H, taken at various temperatures for (a) field applied along the c-axis, and (d) field applied in the ab-plane. Curves are offset by 0.5 μ_BF.U.$^{-1}$ for clarity.

Spin structures of four different magnetic phases of YMn_6Sn_6 are presented in main text Figure 1(d) together with the evolution of the wavevector observed in neutron diffraction experiment. A phase of particular interest is the fan-like phase that shows two wavevectors at k_z = 0.25, and 0.5. Microscopically, the fan-like phase is a commensurate planar structure where the spins in each Mn-layer along the c-axis rotate by angles γ, and δ as: γ, γ, -δ, δ, -γ, -γ, δ, -δ, where $\gamma = 69°$, and $\delta = 12°$[3]. In Supplementary Figure 3 we show schematically the projection of these spins onto the ab-plane: one along the direction of the magnetic field (x-direction), and the other along a perpendicular direction. It can be seen that the spin components along x repeat after four layers (or two unit cells) and those along the perpendicular direction repeat after eight layers (or four unit

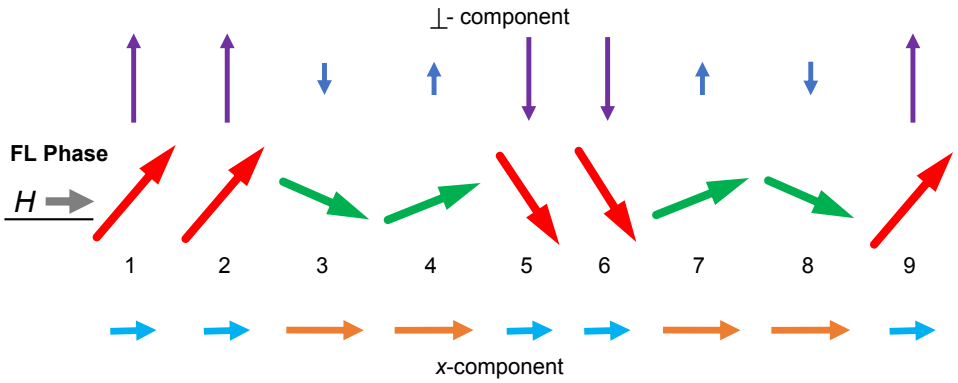

Supplementary Figure 3: Schematic magnetic structure for the fan-like phase by magnetic layer. Breaking up the fan-like phase moments within the ab-plane (center) into perpendicular to H (top) and parallel to H (bottom) components reveals the underlying four unit cell and two unit cell periodicity, respectively. Note each arrow represents the ferromagnetic moments of one Mn-kagome layer. There are two Mn layers per unit cell and the numbers represent layers stacked along the c-axis.

cells) giving rise to the two wavevectors at 0.5 and 0.25, respectively [see supplemental references (2,3) for details].

Supplementary Note 3 Sensitivity of Resistivity to Magnetic Ordering.

Supplementary Figure 4 shows the resistivity of YMn_6Sn_6 as a function of temperature for current (I) both in the ab-plane (ρ_{ab}) (blue), and along the c-axis (ρ_c) (red). While ρ_{ab} gradually decreases on cooling, ρ_c first increases, between 400 and 333 K and then suddenly decreases showing a change in electrical anisotropy concomitant onset of the magnetic ordering. The (0, 0, 1/2) antiferromagnetic ordering of the ferromagnetic Mn planes[5] is consistent with the initial rise in ρ_c where

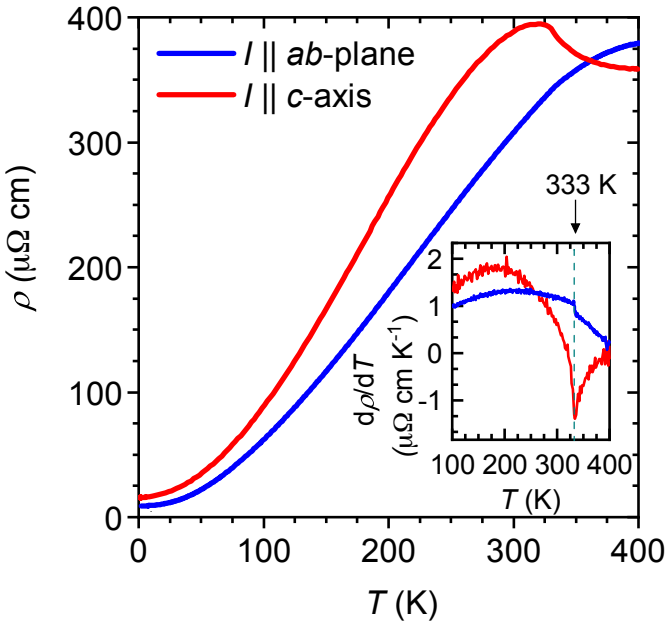

Supplementary Figure 4: Resistivity as a function of temperature, $\rho(T)$, measured with current, I, applied along the c-axis (red line) and in the ab-plane (blue line). The residual resistivity ratios (RRR), defined as RRR$= \frac{\rho(400K)}{\rho(2K)}$ for the c-axis and ab-plane resistivity are 23 and 42, respectively. The temperature derivatives are shown in the inset with the green dashed line emphasizing the sharp transition at 333 K.

the charges moving along the c-axis encounter ferromagnetic planes every two unit cells while the current flowing in the plane moves along the ferromagnetic sheets. Both ρ_c and ρ_{ab} show sensitivity to the onset of the spiral state at 333 K. However, the more pronounced ρ_c drop results from the dramatic change in the angle between the antiferromagnetic planes where they rotate almost 160°, facilitating electron propagation along the c-axis[2].

Supplementary Note 4 Full MR Temperature and Angle Evolution.

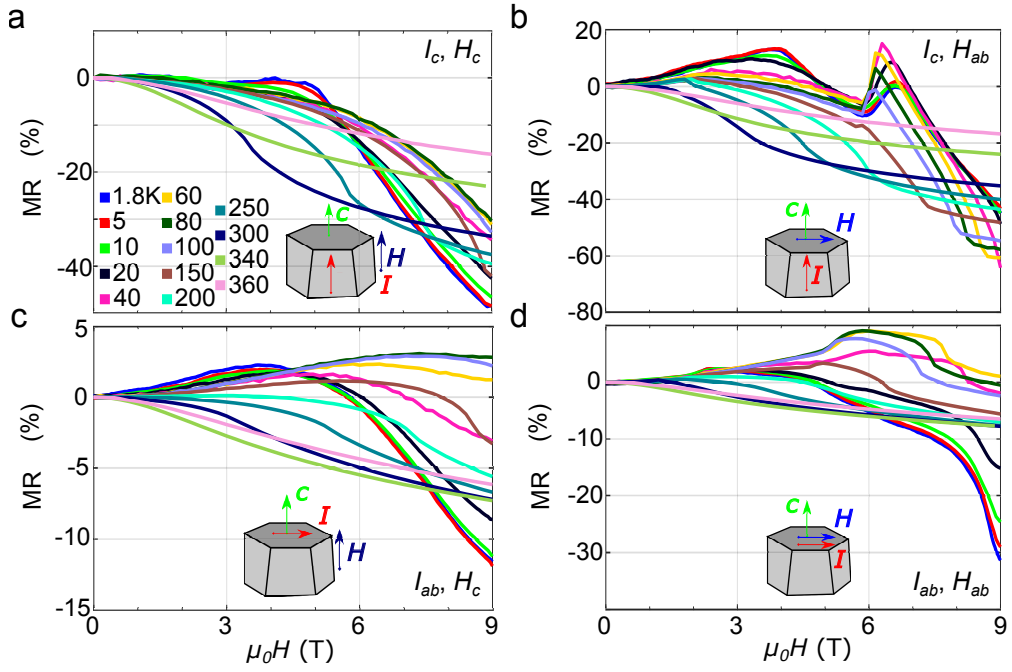

Supplementary Figure 5: Magnetoresistance (MR) at indicated temperatures for the four current and field configurations. Panels (a) and (b) correspond to MR configurations for the current (I) applied along the c-axis with the magnetic field (H) applied parallel and perpendicular to the c-axis, respectively. Panels (c) and (d) correspond to MR configurations for the current applied in the ab-plane with the magnetic field applied parallel and perpendicular to the c-axis, respectively. Schematic diagrams of current, crystal c-axis, and applied field orientations are shown as an inset of each panel. Colors in (b), (c), and (d) correspond to the same temperatures as in (a).

The MR data were taken with four applied fields, currents and sample orientations: resistivity measured along the c-axis and magnetic field applied (1) parallel, and (2) perpendicular to the c-axis, and resistivity measured perpendicular to the c-axis and the field applied (3) parallel, and (4)

perpendicular to the c-axis. Here we present the full temperature dependence of the data shown in Figure 2 in the main text. The data from orientation 1 is shown for all temperatures collected in Supplementary Figure 5(a). The MR in this orientation at 1.8 K is initially negligible for fields up to 5 T, followed by a very steep decline to negative MR as field is increased further. As temperature is increased up to 40 K, this small kink at 5 T, broadens and decreases in magnitude, disappearing completely above 40 K, leaving only a slight monotonic negative MR. At temperatures above 40 K the MR is negative and smooth up to 200 K where a kink develops at high field when the forced ferromagnetic state is reached corresponding with the forced ferromagnetic phase entering within the 9 T range of applied field.

Supplementary Figure 5(b) shows the full temperature dependence of the MR for orientation (2), the same orientation as presented for select temperatures in the main text Figure 3(a). Clearly shown here, as the temperature is increased the 4 T peak broadens and lowers in field and magnitude while the 6.2 T peak maintains its sharpness in field while decreasing in magnitude, disappearing completely at T $>$ 150 K. At high temperatures the distorted spiral to transverse conical spiral transition is clearly indicated by a small low field peak, seen observed here at 2 T at 150 K, and the transverse conical spiral to forced ferromagnetic phase is indicated by a kink in the MR, observed here at 7.2 T at 150 K.

Supplementary Figure 5(c) shows the temperature dependence of the MR for orientation (3). In this orientation, at 1.8 K the MR exhibits an initial rise in response to applied field, turning over at 4 T at a value of 2.2$\%$ MR, and decreasing to a negative MR of -11.6$\%$ at 9 T. The temperature

and field dependence of the signatures in orientation 3 are qualitatively similar to that found for orientation 1. At temperatures 40 K $< T <$ 150 K the initial rise persists and broadens flattening the response until no negative MR is observed at 100 K.

Supplementary Figure 5(d) shows the temperature dependence of the MR for orientation (4). At 1.8 K the field dependence starts with an initial rise up to 2.3% MR at 2.3 T prior to turning over to negative dependence reaching -31.4% MR at 9 T. A small bump is seen at 4 T matching the field for the turnover as see in orientation 2. Unlike orientation 2, however, no sharp peak at 6.2 T is observed at 1.8 K. Instead the MR dependence levels off slightly at 6 T prior to sharply decreasing above 8 T. As temperature is increased to 40 K, the 4 T hump feature broadens and disappears, and a plateau grows from the 6 T feature, leaving a shoulder-like feature in the MR response indicating the fan-like phase transition from the transverse conical spiral phase. Above 40 K, the MR response develops kinks corresponding to the transverse conical spiral to forced ferromagnetic transitions similar to as observed in orientation 2. Above 200 K the dependence is qualitatively the same as in orientation 2 albeit a factor of 7 times smaller in magnitude at 200 K, and a factor of 3 times smaller at 340 K.

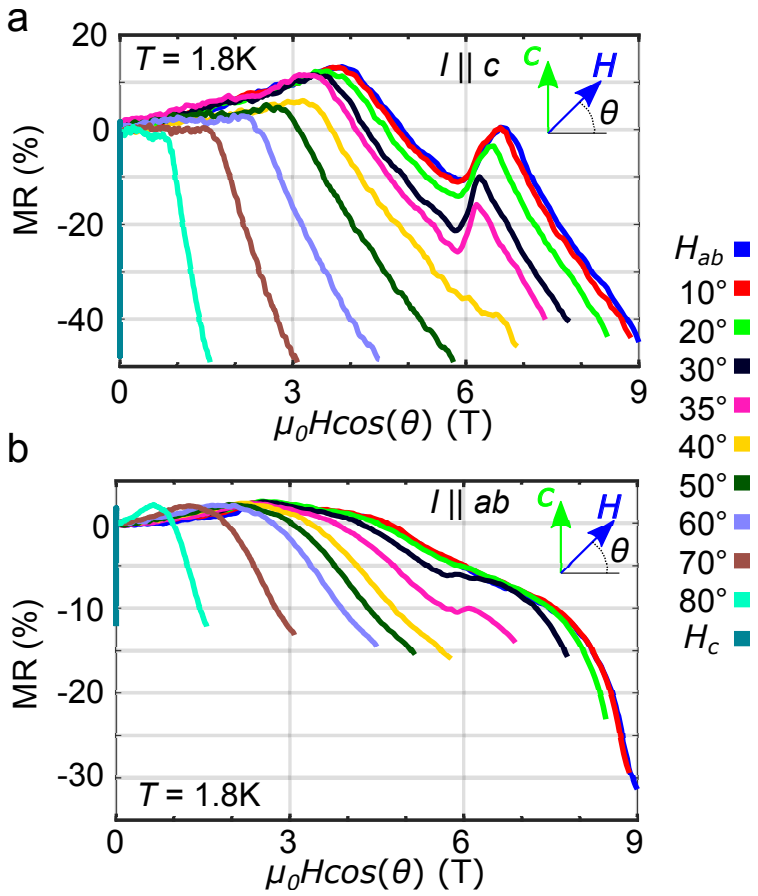

Supplementary Figure 6: Panel (a) depicts the evolution of the MR as a function of the in-plane field component as the applied field is rotated from configuration 1 to configuration 2 at T $= 1.8$ K. Panel (b) depicts the evolution of the MR as a function of the in-plane field component as the applied field is rotated from configuration 3 to configuration 4. Angles for (a) and (b) are measured from the ab-plane with 0° corresponding to field in-plane and 90° corresponding to H parallel to the c-axis.

The $T = 1.8$ K dependence of the MR response on the in-plane field component for various applied field angles is compared for current along the c-axis and in the ab-plane in Supplementary Figure 6(a) and (b), respectively. The plots depict MR dependence as a function of $\mu_0 H cos(\theta)$,

where θ is the angle made by the magnetic field with the basal plane. Comparing the two current orientations, both show more complex features with field in-plane than with field applied along the c-axis as expected based on the magnetization. However, with the current out-of-plane the features are much more prominent and sharper, supporting the interplanar MR as a much better probe for the field dependent transitions. As observed in Supplementary Figure 6(a) and (b), the MR drop at H' persists at all angles. The H_2 MR peaks, however, disappear when the applied field angle is at or exceeds 40°. At 40°, our applied field strength of 9 T is still able to reach this critical in-plane field component, however the H_2 MR peak disappears, indicating that at 40° and above the H parallel to c component is driving the magnetic transitions. Also, the H_2 peaks line up approximately to the same value of the in-plane component of the magnetic field ($Hcos(\theta) \approx$ 6.2-6.5 T). These observations suggest that the 10% increase in MR forming the H_2 peak is associated with the formation of the fan-like phase that develops only when the magnetic field is below a critical angle between 35° and 40° of the ab-plane.

Supplementary Note 5 Thermal Conductivity

Supplementary Figure 7 shows thermal conductivity (κ) of YMn_6Sn_6 as function of temperature where we see that κ peaks at 38 K and sharply decreases below this temperature. This sharp decrease is evidence of the phonons being frozen out at lower temperatures leaving the electrical contribution to the thermal conductivity as the primary source of heat carriers. The thermal conductivity was measured via the Quantum Design PPMS Thermal Transport Option (TTO) where the sample was polished to a rectangular bar and mounted with the standard TTO thermometer

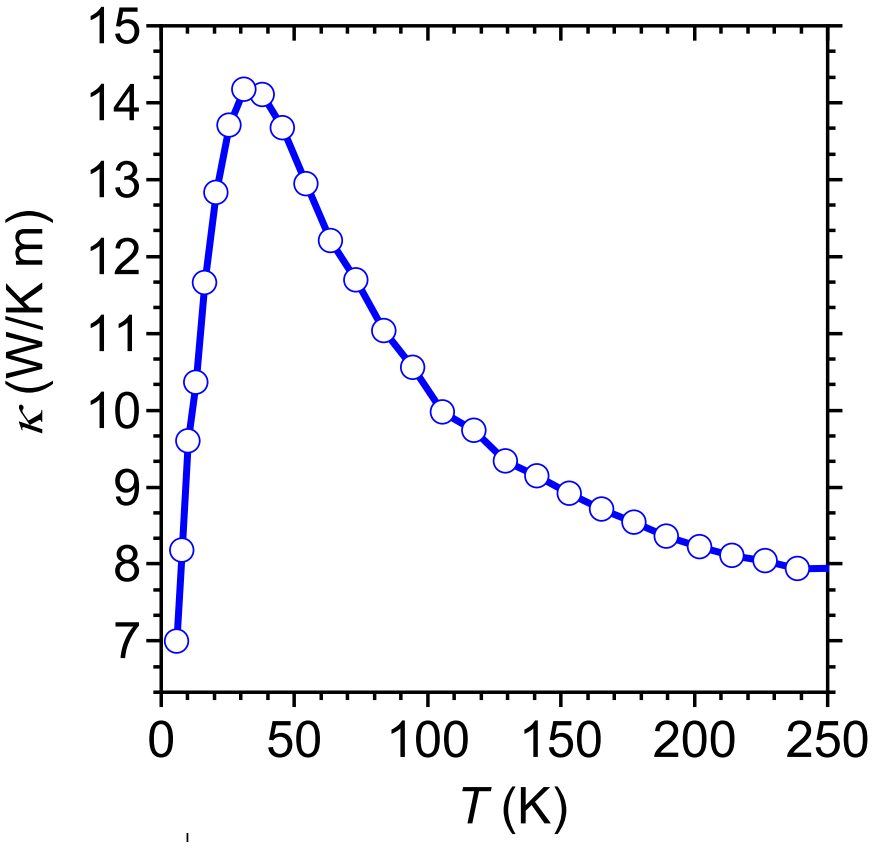

Supplementary Figure 7: Thermal conductivity (κ) of YMn_6Sn_6 as a function of temperature.

shoes. The sample geometry yielded a cross-sectional area of 0.307 mm^2 with thermometer lead separation of 1.205 mm. The applied heat current was directed within the ab-plane of the sample with the heat pulses maintained at 3% of the sample temperature for each temperature setpoint measured.

Supplementary Note 6 DFT: All Electronic Bands.

All calculated bands for the spiral ground state and for the spin up and spin down polarized states are shown in Supplementary Figure 8. The nearly flat band at the L point forms in the spin up

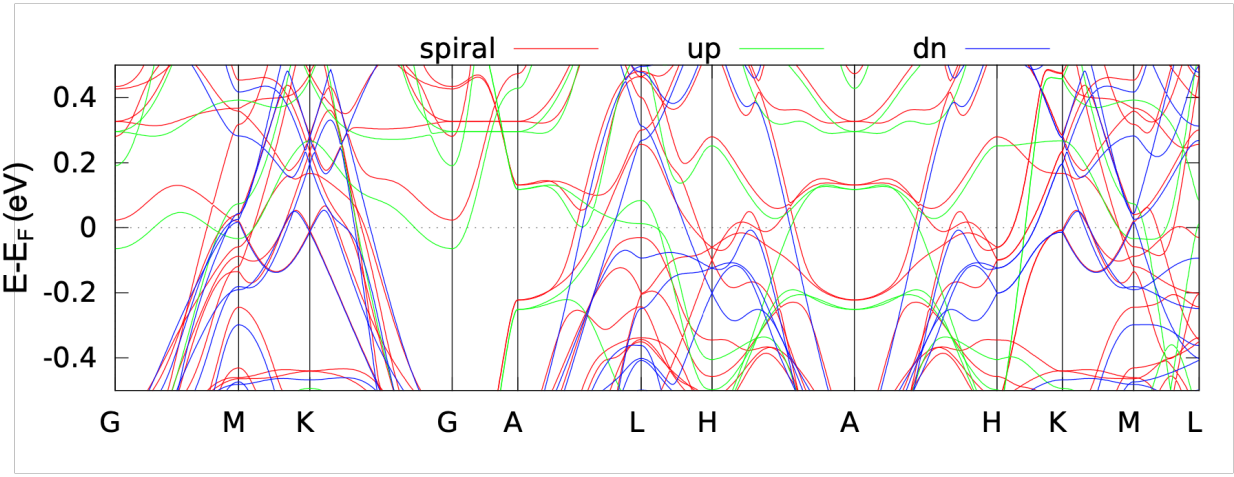

Supplementary Figure 8: All electronic bands calculated for the spiral state (red), spin up (green) and spin down (blue).

channel (shown in green). The Dirac point in the spin down channel (shown in blue) is located approximately 50 meV below E_{F} at the K point.

Supplementary Note 7 Full Hall temperature evolution.

The Hall resistivity for the full range of temperatures measured is presented in Supplementary Figure 9(a) and (b) for current in the ab-plane, and along the c-axis respectively. No signature at H' is seen in the Hall data as is seen in the MR field dependence at low temperatures. The full range of temperatures here are in agreement with previously published Hall results[2].

Regarding the absence of a marked change in conductivity at the LT presented in the main text, it is natural to expect that in a metal with complex fermiology, any transport property is affected by all Fermi surface pockets in a complex way. Ordinary Hall conductivity, σ_{H}, originating

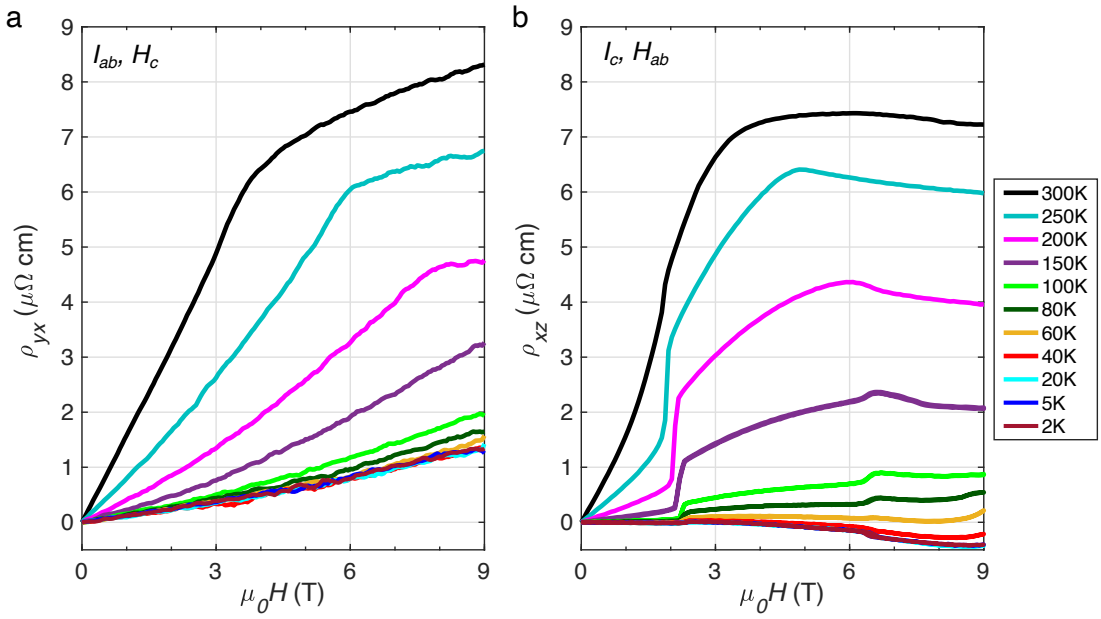

Supplementary Figure 9: Hall resistivity vs applied field for all measured temperatures. Panel (a) shows the configuration with current applied in the ab-plane and field along the c-axis and panel (b) shows the configuration with current applied along the c-axis and the field applied in the ab-plane.

from a nascent pocket can be estimated by the standard formula[6,7],

$$\sigma_{\mathrm{H}} \propto \left\langle N(E_{\mathrm{F}})\mathbf{v}_{\mathrm{F}} \cdot [\mathrm{Tr}(\mathbf{M}^{-1}) - \mathbf{M}^{-1}] \cdot \mathbf{v}_{\mathrm{F}} \right\rangle, \tag{SI1}$$

where N is the density of states, E_{F} is the Fermi energy, v_{F} is the Fermi velocity, $\mathbf{M}$ is the effective mass tensor and the averaging is performed over the Fermi surface pocket. It is easy to see that for a pocket with the effective dimension D, the $N(E_{\mathrm{F}}) \propto k_{\mathrm{F}}^{D-2}$, and σ or $\sigma_{\mathrm{H}} \propto k_{\mathrm{F}}^{D}$ (k_{F} is the Fermi wavevector). Thus, while the 1D DOS is diverging at an LT, the conductivities vanish. Therefore, in a multiband system such a transition can be easily shadowed by other bands with large ordinary Hall conductivities.

As a simple illustration, let us consider the case of a two-band system. The general formula for the Hall coefficient in the Boltzmann approximation is given by:

$$R_{\rm H} = (\sum \frac{\sigma_i^2}{n_i^H})/(\sum \sigma_i)^2, \tag{SI2}$$

where σ_i = $e^2(n/m)_i\tau_i$ is the electrical conductivity in the i^{th} band. n_i, m_i, and τ_i are carrier concentration, mass and Boltzmann relaxation time, respectively. In a two-band system [taking $e = 1$, and $(\tau/m)_i = D_i$]

$$\sigma = \sigma_1 + \sigma_2 = n_1 D_1 + n_2 D_2, \tag{SI3}$$

and,

$$R_{\rm H} = \frac{(\sigma_1^2/n_1 + \sigma_2^2/n_2)}{(\sigma_1 + \sigma_2)^2} = \frac{n_1 D_1^2 + n_2 D_2^2}{(n_1 D_1 + n_2 D_2)^2}. \tag{SI4}$$

Then,

$$\frac{d\ln\sigma}{dn_2} = \frac{D_2}{n_1 D_1 + n_2 D_2}. \tag{SI5}$$

Or,

$$\left.\frac{d\ln\sigma}{dn_2}\right|_{n_2\to 0} = \frac{D_2}{n_1 D_1}. \tag{SI6}$$

And,

$$-\frac{d\ln R_{\rm H}}{dn_2} = \left(\frac{D_2}{n_1 D_1 + n_2 D_2}\right)\left[1 - \frac{n_1 D_1 (D_2 - D_1)}{n_1 D_1^2 + n_2 D_2^2}\right]. \tag{SI7}$$

Or,

$$-\frac{d\ln R_{\rm H}}{dn_2}\Bigg|_{n_2\to 0} = \left.\frac{d\ln\sigma}{dn_2}\right|_{n_2\to 0}(2 - \frac{D_2}{D_1}). \tag{SI8}$$

Note: Here the derivative is taken with respect to n_2 and set it to zero to account for the fact that the second pocket has just opened up and is much smaller compared to the first pocket. Equa-

tion SI8 shows that $-\frac{d\ln R_{\rm H}}{dn_2}\Big|_{n_2\to 0}$ can be many times smaller than $\frac{d\ln\sigma}{dn_2}\Big|_{n_2\to 0}$ because of potential cancellation in $(2-\frac{D_2}{D_1})$.

Supplementary Note 8 Inter-Layer Hopping.

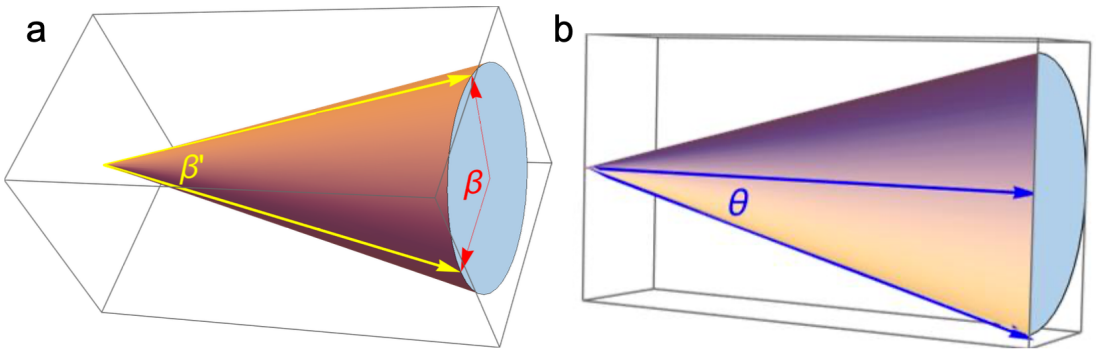

Supplementary Figure 10: Notations for angles used in the calculations of the hopping parameter for the transverse conical spiral phase. (a) β and β' angles between two spins in consecutive planes in the transverse conical spiral phase. (b) conical angle θ describing the cone which the spins spiral around in the transverse conical spiral phase.

Let us now consider the transverse conical spiral. The conical angle θ we will estimate from the formula,

$$M_x = M_{\rm sat}\cos(\theta). \tag{SI9}$$

Taking $M_{\rm sat}\approx 13.1\ \mu_B{\rm F.U.}^{-1}$ and $M_x\approx 9.8\ \mu_B{\rm F.U.}^{-1}$, we get $\theta\approx 43^\circ$. Next, we recall that the spiral angles stagger so that, at $H=0$ and $T=0$, the magnetization rotates between the planes intercalated by Sn_3 by an angle α and between those intercalated by Sn_2Y by β. As H is increased, the spins cant in the direction of the field, and the angles are, in the first approximation, independent

of H (they are defined by the ratios of the exchange couplings, but not by their magnitudes).

We can then calculate the rotation angles between the two consecutive planes, α' and β', as a function of the canting angle, assuming the two spiral angles α and β remain the same as at $H = 0$, that is, -20° and 110° (the relation between primed and unprimed angles, and θ, are illustrated in Supplementary Figure 10). Then,

$$\alpha' = \cos^{-1}(\cos^2\theta + \sin^2\theta\cos\alpha) \approx 13.6^\circ, \tag{SI10}$$

$$\beta' = \cos^{-1}(\cos^2\theta + \sin^2\theta\cos\beta) \approx 67.9^\circ. \tag{SI11}$$

The "hopping bottleneck" will be $\cos(\beta'/2) = 0.83$.

Let us now consider the fan-like phase. Previous work[3] has quantitatively characterized the fan-like magnetic structure of YMn_6Sn_6 at the transverse conical spiral–fan-like phase boundary. To a good approximation, the every-other hopping step does not involve spin rotation, and the other half involves rotations by $\gamma + \delta = 69^\circ + 12^\circ = 81^\circ$, giving the bottleneck factor $\cos((\gamma + \delta)/2) = 0.76$ [we are using the "model 2" from Ref. (3)]. Since the conductivity is roughly proportional to the effective hopping, we can estimate that transitioning into the fan-like phase should increase the resistivity by 0.83/0.76$\sim 9\%$, in good agreement with the experiment. It should be mentioned that this good agreement may be fortuitous, because the approximations used in the estimation above are rather semiquantative, but, in any event, they indicate that the assumed physical model is clearly compatible with the experiment.

Supplementary References.

1. A. Aharoni Demagnetizing factors for rectangular ferromagnetic prisms. *Journal of Applied Physics* **83**, 3432 (1998).

2. Ghimire, N. J. *et al.* Competing magnetic phases and fluctuation-driven scalar spin chirality in the kagome metal YMn_6Sn_6. *Science Advances* **6**, eabe2680 (2020).

3. Dally, R. L. *et al.* Chiral properties of the zero-field spiral state and field-induced magnetic phases of the itinerant kagome metal YMn_6Sn_6. *Physical Review B* **103**, 094413 (2021).

4. Uhlíová, K. *et al.* Magnetism of YMn6Sn6 and DyMn6Ge6: Single-crystal study, *in WDS'06 Proceedings of Contributed Papers Part III (Matfyzpress, 2006)* pp 48–53 .

5. Zhang, H. *et al.* Topological magnon bands in a room-temperature kagome magnet. *Physical Review B* **101**, 100405 (2020).

6. Hurd, C. The Hall effect in metals and alloys. *Plenum Press, New York* (1972).

7. Schulz, W. W. *et al.* Hall coefficient of cubic metals. *Physical Review B* **45**, 10886 (1992).